Planar Near-Field Array Antenna Diagnostics for Production Testing Using Compressive Sensing and a Fixed Sparce Sensing Array

Clive G. Parini, *Member, IEEE*, Stuart F. Gregson

***Abstract*— In massive MIMO arrays, Compressive Sensing (CS) has been proposed to rapidly verify the arrays excitation in a production environment. All follow the general approach of creating the sparsity needed for CS by subtracting the measured far-field or near-field of the test array from that of a 'gold standard' array measured under identical conditions. In several previous papers the authors have applied CS to planar near-field (PNF) measurements with a view to building a compact test facility well suited to the production environment for these antennas. In this paper we identify a fundamental flaw in the creation of the difference pattern between a gold standard antenna and the test antenna, in that the electrical path length difference between probe and gold standard antenna and that of probe to test antenna must be no more than 0.002λ or 0.7°. Even if mechanical tolerance can achieve this, thermal drift in the RF subsystem will easily reach the 0.7° figure. The paper then describes an analysis process that overcomes this problem restoring the CS process to very nearly the levels of performance described in our previous publications and those of other workers. To achieve this, we have used a fixed set of NF probes located randomly over a region confined to the central part of the NF measurement plane along with a PIN switch matrix to offer a very rapid and very consistent RF measurement. We have extensively simulated a massive MIMO array of 8x24 elements and found that just 25 NF probes can detect up to 2% failure rate. In addition, we present a technique to improve the accuracy of the array excitation reconstruction by using several partial excitations of the array. In this work we consider both array element amplitude and phase reconstruction performance and demonstrates that it is possible to detect a single element, phase only, fault of just 22.5°.**

***Index Terms*— Compressive Sensing, Sparse Sampling, Massive MIMO, Antenna Measurements, Antenna Metrology, Array Antennas, Planar Near-Field Measurements, Planar Near-Field Array Diagnostics.[1]**

I. Introduction

THE enormous increase in data throughput required by modern communication systems has necessitated the adoption of several new technologies. Perhaps the most significant of these concerns the shift to higher frequency bands, and the use of array antenna architectures, specifically Massive MIMO (Multiple Input Multiple Output) antennas employing electronic beam shaping and scanning. Although the shift to the FR2 band is perhaps happening more slowly than was first anticipated, the proliferation of more complex, electrically large, massive MIMO antennas [1, 2] with their complex phased array topologies, comprised of many thousands of individually controlled radiating elements, greatly complicates the test, calibration, and measurement aspects of the production process. Historically, the techniques that were developed for high value, low volume production, of electronically scanned arrays used in aerospace or space applications were time consuming and are generally considered to be inappropriate for applications requiring mass manufacture of many tens of thousands of units. These techniques generally include using a single low scattering probe to sample the electric field close to each array aperture, *i.e.* to park-and-probe, the array, or the use of microwave holographic metrology (MHM) [3], and aperture diagnostics to verify the element excitations [3, 4]. The cost, complexity and time required by these approaches are such that they are rendered inappropriate for use in modern volume production environments such as those that are commonplace in the manufacture of user equipment and/or Group Radio Access Networks. This is the motivation for this work which seeks to find practical methods for the acceleration of production test and calibration of massive MIMO arrays.

Modern CS considers the problem of reconstructing signals that have been sampled at sub-Nyquist rates with the condition that they be sparse or compressible in some domain with the grounds of this work being published in 2006 in [5, 6, 7]. Typically, this sort of problem is constructed as a linear inverse problem which classically would be tackled by determining the Moore-Penrose pseudoinverse. This is possible providing the number of equations outnumbers the number of unknows. If this is not the case, then the system is underdetermined, the inverse problem is ill posed and has no unique solution. However, if we add the constraint that the signal, in some domain, has only a few non-zero elements, *i.e.* is sparse, then under this assumption, it is mathematically possible to reconstruct the sparse signal thereby solving the optimisation problem. Unfortunately, this problem is of combinatorial nature and is computationally intractable [8]. However, if the problem is relaxed to the convex l_1-minimisation problem, then an efficient solution can be found. A condition for the guaranteed recovery can be provided by satisfying the Restricted Isometry Property (RIP) [5, 6, 7] which introduces the requirement for

Clive G. Parini are with the School of Electronic Engineering and Computer Science, Queen Mary University of London, E1 4NS London, UK (e-mail: c.g.parini@qmul.ac.uk).

Stuart F. Gregson is with Next Phase Measurements, Garden Grove, USA, and the School of Electronic Engineering and Computer Science, Queen Mary University of London, London, UK (e-mail: stuart.gregson@qmul.ac.uk).

random sampling and adoption of parsimonious solution [9].

Compressive Sensing (CS) has been successfully deployed in a range of applications and is predicated on the principle that it is possible to reconstruct a large space (*P*), from merely a few samples (*S*) providing that we can find an appropriate transform that enables the large space to be defined by a few elements within this mostly empty, *i.e.* sparse, domain. For the case of antennas and antenna measurements, an array of elemental radiating sources can be employed to specify the far-field radiation pattern function. When using the Green's function based equivalent sources method, the transform from the NF to antenna aperture can be harnessed to provide the 'compressed sensing' protocol. Here, the key to CS being the recovery of the complete measurement from the sparsely sampled randomly distributed measurements [10].

CS was first applied to the spherical near-field (SNF) case to reduce the number of NF measurements needed by exploiting the inherent sparsity property within the spherical mode coefficients when acquired within an appropriate frame of reference [11, 12, 13] and thereby decreasing measurement times with a reduction in the number of SNF measurement points. CS techniques have also found utility in Inverse Synthetic Aperture Radar (ISAR) target imaging [14] where the approach was found to provide a very efficient way of evaluating measured target signatures located within SAR backgrounds enabling the identification of target signatures. CS based processing has found utility as a way of further enhancing mode-filtering based far-field scattering suppression techniques [9]. Here, the CS method was used to recover the antenna cylindrical mode coefficients (CMCs), which is tenable because of the coordinate translation of the measurement pattern to the rotation centre, resulting in the CMCs become quite sparse in the mode domain. This extends the generality of the mode filtering method to include under-sampled data, and data acquired at positions which grossly deviate from the typically equally spaced abscissa.

Returning to the question of array diagnostics and fault detection of planar array antennas, *i.e.* the most frequently encountered class, classically one would gravitate towards utilising a planar measurement approach and a plane-wave spectrum-based post-processing technique [3, 15]. However, the sort of sparsity afforded naturally by the spherical and cylindrical mode domains for an antenna centred expansion is *not* available in the plane-wave spectrum [9]. Instead, an alternative approach must be sought [16, 17]. Here, instead of relying on the sparsity provided by the coefficients of the specific modal expansion being utilised for the representation of the particular radiator, we instead reduce the number of measurement points required for NF to FF transformation by assuming that the number of failed elements within the array was far smaller than the total number of elements within the array. This was found to be a crucial step in providing the requisite sparsity property to enable compressive sensing to be successfully deployed. However, this technique requires the availability of a reference, *i.e.* a properly functioning 'gold' antenna and imposes upper bound limitations upon the stability of the measurement system, the repeatability and reproducibility of the measurements, as well as the sensitivity, *i.e.* the amount of measurement noise permissible.

In this paper, we exploit the fact that in a production test setting a 'gold' reference antenna exists, and explore the use of CS to undertake a back transform to the array aperture from a planar measurement of the *difference* between the NF pattern of the AUT and the 'gold' antenna, using a minimal number of randomly located NF measurements where the locations are preserved between the gold and production antenna tests. Thus, the desire is to minimise the number of measurement points required to reliably recover the radiating elements' complex excitations. Thus, the approach used in this paper can be seen presented in Fig. 1 below where the back propagated aperture field indicates the *difference* between the aperture field of the "faulty", *i.e.* defective, production antenna, and the ideal 'gold' reference antenna.

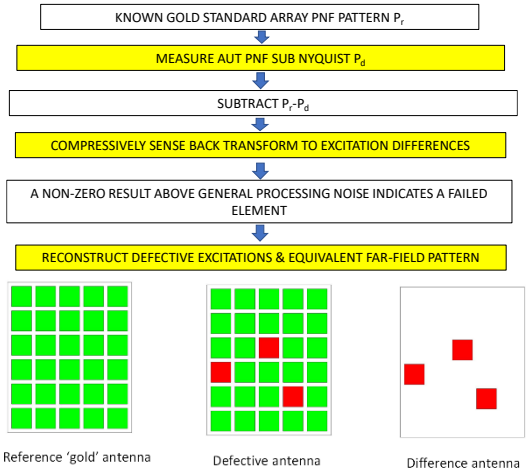

Fig. 1. Top: Flow diagram of defective element detection using compressive sensing. Bottom: the 'sparse' difference antenna concept

II. Overview of the Equivalent Currents Method

The equivalent magnetic current approach utilises a Green's function based methodology to obtain an equivalent magnetic current sheet over a convenient surface that encloses the AUT from the complex EM field acquired over a two-dimensional surface in front of some radiator. Once the equivalent currents (EC) have been determined, they can then be used to propagate the electric fields elsewhere in space including to the far-field [3]. In this procedure, an electric field integral equation (IE) is set-up which relates the measured near electric fields to a set of equivalent magnetic currents which can be solved using an efficient yet very resource intensive method of moments procedure [3, 15]. This typically involves a point matching technique which converts the IE into an equivalent matrix equation, allowing it to be solved in one of several ways, *e.g.* by determining the Moore-Penrose pseudoinverse or from the least squares conjugate gradient (LSQR) method [3, 15]. The above is just one flavour of the wider subject of inverse source methods that can be applied to reconstruct to arbitrary surfaces and a good introduction to this whole subject can be found in chapter 9 of [15], along with [23, 24]. A detailed treatment of the EC method that is employed for this work can be found in can be found presented in [3,18] and instead only a brief

overview is presented herein.

Let us assume that the radiator is placed in the negative *z*-axis half-space and is radiating forward into the positive *z*-axis half-space, with the two regions bounded by an infinitely large *xy*-plane. If we introduce an infinite perfect electric conducting (PEC) sheet on one side of the surface, then in this case only the tangential components of the electric fields need be specified on the surface. Thus, by using the image theorem, the magnetic current can, for an antenna with a well-defined aperture, be expressed approximately as [3, 15, 18],

$$\underline{J}_m(\underline{r}') = \begin{cases} 2\left(\underline{E}_a(\underline{r}') \times \hat{\underline{n}}\right) & \text{over the aperture} \\ 0 & \text{elsewhere} \end{cases} \tag{1}$$

Since the radiated fields must be determined in the presence of the conducting sheet, this results in the solutions only being available for the forward half-space. The electric vector potential $\underline{F}$ may be defined in terms of the integral of this equivalent current as [3, 15, 18],

$$\underline{F}(\underline{r}) = \frac{\varepsilon}{4\pi}\int_S \frac{\underline{J}_m(\underline{r}')}{R} e^{-jk_0 R} ds' \tag{2}$$

Here, primed variables are associated with the source point, un-primed variables are associated with the field point, the free-space propagation constant is denoted by k_0, and the displacement R can be expressed as,

$$R = |\underline{r} - \underline{r}'| = \sqrt{(x-x')^2 + (y-y')^2 + (z-z')^2} \tag{3}$$

Since we can obtain the electric fields from the electric vector potential $\underline{F}$ using [3, 15, 18],

$$\underline{E}(\underline{r}) = -\frac{1}{\varepsilon}\left(\nabla' \times \underline{F}(\underline{r}')\right) \tag{4}$$

Then,

$$\underline{E}(\underline{r}) = \frac{1}{4\pi}\int_S \underline{J}_m(\underline{r}') \times \nabla' g(\underline{r}, \underline{r}') ds' \tag{5}$$

Here, $\underline{J}_m$ denotes the surface magnetic current sheet that we seek, $g(r,r')$ the Greens function and $\underline{E}(\underline{r})$ is the electric field that is measured across the planar near-field measurement surface *S*, which is located at a distance of a few wavelengths from the AUT. This is a typical dimension required to minimize reactive coupling and AUT-to-probe multiple reflections [3]. If we assume a Cartesian coordinate system and polarization basis, we may write this in a more convenient form as [3, 15, 18],

$$E_x(\underline{r}) = \frac{1}{4\pi}\int_S \frac{e^{-jk_0 R}}{R^2}(z-z')\left(jk_0 + \frac{1}{R}\right) J_{my}(\underline{r}') ds' \tag{6}$$

$$E_y(\underline{r}) = \frac{-1}{4\pi}\int_S \frac{e^{-jk_0 R}}{R^2}(z-z')\left(jk_0 + \frac{1}{R}\right) J_{mx}(\underline{r}') ds' \tag{7}$$

Here we employ the field equivalence principle (*represent the field at an arbitrary point in space as an integral over the surface on which the fields are known*) and use just the tangential field on the measurement plane to fully characterise the field everywhere. This integral equation can be solved using a method of moments (MoM) approach [3, 15, 18]. Here, we can utilize the sampling theorem to replace the continuous current sheet with an array of fictitious magnetic dipoles, and the electric fields with a set of discrete samples. This is equivalent to using a Dirac delta function for the expansion of the current sources and enables us to replace the integration with a summation. Thus, this allows us to express this as a system of linear equations, which we may express in matrix form as,

$$[E_x] = [G][J_{my}] \tag{8}$$

$$[E_y] = -[G][J_{mx}] \tag{9}$$

Here, the elements in the matrix [G] can be populated by evaluating numerically the integral,

$$G_{k,l} = \frac{1}{4\pi}\int_{S_{k,l}} \frac{e^{-jk_0 R}}{R_{k,l}^2}(z_k - z_l')\left(jk_0 + \frac{1}{R_{k,l}}\right) ds' \tag{10}$$

Providing the reconstructed currents are *more* than a wavelength away from the measurement surface, as they will be in the case of a near-field measurement, then the area of integration may collapse to that of an infinitesimal current element. Thus, the coefficients for the fictitious magnetic dipole array can be obtained by solving [3, 15, 18],

$$[G]^{-1}[E_x] = [J_{my}] \tag{11}$$

$$[G]^{-1}[E_y] = -[J_{mx}] \tag{12}$$

Crucially, this system of equations is in a form that is amenable for treatment by the CS method.

As in a practical PNF measurement E_x and E_y would be determined using a probe antenna and to recover the true E_x and E_y probe pattern correction would be required [3]. For the purposes of our simulation, we assume a perfect Hertzian dipole probe which requires no probe pattern correction. This in no way compromises the simulation and avoids the need to first simulate the PNF measurement with a real probe and then remove its effect to recover the true E_x and E_y field.

III. Use of CS in The Detection of Defective Radiating Elements

As described above, in this CS application we assume the availability of the failure-free reference 'gold' array antenna [3, 4, 16, 17], comprised of *N* radiating elements' excitation coefficients are defined as $X_r = \{x_1, \ldots, x_n, \ldots x_N\}^T$, where x_n is the excitation coefficients of the n^{th} radiating element. The corresponding near-field pattern vector is denoted as $P_r = \{p_1, \ldots, p_m, \ldots, p_M\}^T$, where p_m is the probe voltage measured at the m^{th} NF sampling point of a total of *M* sample points. Similarly, we can denote X_d as being the excitations of the (defective) AUT collected at sub-Nyquist sampling rate, and P_d as the probe measured near-field pattern collected from the AUT. Thus, we may consider the following system of equations where [10],

$$P = AX + \varsigma \tag{13}$$

where $P = P_r - P_d$, $X = X_r - X_d$, $\varsigma(0, \sigma^2)$ is additive white Gaussian noise (AWGN) with zero mean and variance σ^2 and is controlled by specifying a signal-to-noise ratio for the measurement. It is important to note that both P_r and P_d are sampled at the same locations and at a sub-Nyquist rate. As stated in the previous section the equivalent currents formulation of (11) and (12) is of the form of (13) where *P*

relates to E, X to J and A to ψG with the binary sampling matrix $\psi \in C^{M\times K}$ selecting M rows randomly from the G matrix with elements defined by (10) and $G \in C^{K\times N}$.

The purpose of array diagnosis is to detect the faulty elements. We denote the number of faulty elements as F, which is assumed to be much smaller than the number of radiating elements N. Thus, X is an F-sparse vector in which only the faulty elements of the original array contribute to the sparse vector. Thus, we have successfully converted the problem into a sparse one. The standard CS technique can be used to recover X_d with the knowledge of the excitation coefficients of the 'gold' antenna, X_r, by solving the following problem [3, 10],

$$\min_X \|X\|_0 \quad s.t.\ \|P - AX\|_2 < \sigma^2 \tag{14}$$

where σ^2 is determined by the noise level affecting the measured samples P_d and P_r. Here it is noted that the l_0 problem is non-convex and difficult to solve. In compressive sensing, it has been relaxed to an l_1 problem with guarantee on exact recovery when RIP is satisfied [10]. Therefore, the optimization problem is relaxed to,

$$\min_X \|X\|_1 \quad s.t.\ \|P - AX\|_2^2 < \sigma^2 \tag{15}$$

The above l_1 problem is convex, which could be solved by standard convex optimization tools. The overall procedure of CS based defective array detection can be seen illustrated in Fig. 1. A comprehensive discussion of the CS principle is beyond the scope of this paper. More information is available in the open literature, *e.g.* [10]. To efficiently solve (15), several software packages are available, *e.g.* CVX [19], YALL1 [20], and SPGL1 [21] which are all readily accessible and can be deployed. For this study, we have chosen to utilize the YALL1 algorithm due to its desirable balance of efficiency and accuracy [3]. Clearly, the CS process can be directly applied to a one-dimensional linear array, where X_d is the recovered excitations. However, this can be easily extended to the two-dimensional array case where we reorder the two-dimensional array of excitations into a one-dimensional vector whilst managing the correct phase relationship between two-dimensional elements and NF radiation. For example, an 8 x 24 element array X_d has 192 elements, and in the following sections we will show the application of CS for two-dimensional array diagnosis. Of course, the assumption here is that we know a priori the excitations of the gold antenna, X_r from which we can derive X_d and then subsequently the corresponding far-field pattern, where in practice X_r can be determined from an auxiliary measurement, computational electromagnetic simulation, *etc*. To get the maximum performance from the CS algorithm we need to minimise the number of unknown coefficients X, these being the number and location of the fictitious magnetic dipoles over the array aperture. This is best achieved by matching their location to the physical location of the centre of each array element and is hence the only required a-priori information, along with the location of the array surface relative to the planar NF scan.

IV. CS Reconstruction Performance

In our previous work on NF CS, we considered the simulated diagnosis of a large 20x28 = 560 element array and in [4, 17] we gave an indication of the performance achievable. If the array had an expected failure rate of *circa* 1% (6 faults in this case) then we needed to take around 183 samples (1.5% of Nyquist sampling needed for classical back projection). Here Nyquist sampling for planar near-field is defined as having data point spacing of finer than half-wavelength across the measurement plane which itself is specified in relation to the desired far-field maximum pattern angle and AUT-to-probe separation distance [3]. However, if we were expecting a failure rate of 4% (22 faults) then we needed to take a larger number of around 380 samples (3.1% of Nyquist). This array had an element spacing of 0.41λ and in this paper we aim to investigate how scalable these results are for a smaller massive MIMO array (8x24 = 192 elements), but one that has larger array element spacing (0.5λ x 0.7λ). If we aim for a fault detection level of at least 2% (4 faults), then Fig. 2 shows how a set of four faulty elements (with fault levels shown inset to figure) effects the far-field (FF) pattern of an array with intended excitation of uniform amplitude and phase.

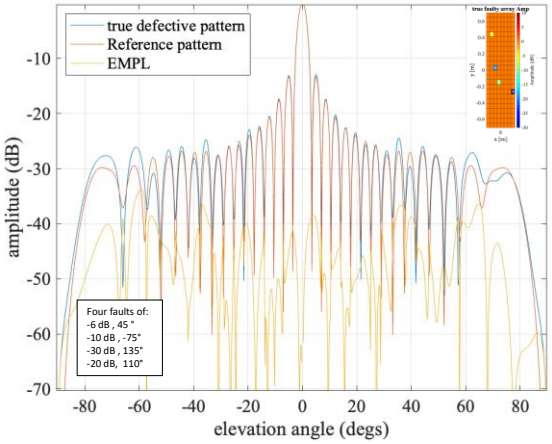

Fig. 2. Radiation pattern of 8x20 array with and without 4 randomly located faults of the type shown in the inset box.

For this work, and our previous work reported above, all our simulation of the measured NF includes the fact that the RF system will add -60dB of noise relative to the peak NF signal. In addition, all the faults in our simulations are of the amplitude and phase form shown inset to Fig 2, unless otherwise stated in the specific simulation. Specifically, the types of faults included do not merely represent the binary change of turning off given elements, but rather include the case of incorrectly set amplitudes and or phases which are more representative of reality. In addition, we also address the important case of purely phase errors as these tend to be more deleterious to the ensuing far-field pattern.

It is clear from this FF pattern cut that any attempt of detecting this low level of fault by looking at the FF pattern would be fruitless. Also shown in Fig. 2 is the equivalent multipath level (EMPL) [3], *i.e.* the difference between the faulty pattern and the *gold* antenna, with an average EMPL of -46 dB and a gain loss of 0.16 dB for 4 random faults. As in our

previous work, we use a statistical measure of reconstruction performance based on plotting the cumulative distribution function (CDF) [3, 4] of the rms error of the reconstructed array amplitude excitation over 50 runs of randomly located faults with a fixed set of randomly located sample points.

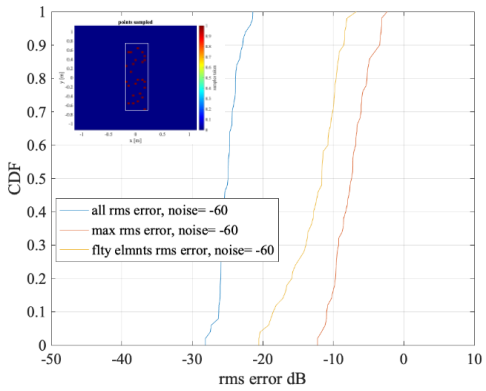

Fig. 3. CDF of the rms array excitation error over 50 runs for the case of 4 randomly located amplitude and phase faults of the form shown inset to Fig. 2. Also shown inset is the 25 pseudo randomly located samples contained with the projection of the array aperture in the sampling plane.

Fig. 3 shows the CDF result for the case of 4 faults of the type shown in Fig. 2 with just 25 pseudo random samples located within the 3λ spaced NF measurement plane, with the NF samples contained within the boundary defined by the projection of the array aperture in the NF measurement plane (white square bounding the red sample points shown inset to Fig. 3). Here, the blue trace represents the RMS error level of the amplitude excitation viewed across the whole array, the red trace shows the maximum RMS error excitation across the elements, and the yellow trace shows the maximum value of the RMS excitation error across *just* the faulty elements ("flty elmnts") within the array, *cf.* [4].

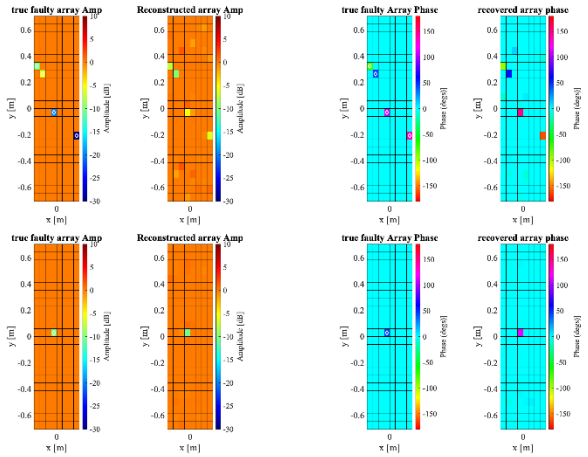

Fig. 4. Typical level of amplitude and phase reconstruction for 25 NF samples, top the case of Fig. 3 with 4 faults; Bottom the case for 1 fault.

As in our previous CS work, we assume the RF system will add -60dB of noise relative to the peak NF signal and this is true for all the simulated measurements presented in this paper. The results of Fig. 3 are repeatable if we let both the sample locations and the fault locations be randomly chosen. Similar results are also seen over a wide range of values for the σ parameter in (15). We have found this agreement to be true for all the other CDF results presented in the paper but have, due to the constraints of available space, chosen just to present here the case of fixed sample points and random fault location as this is how the production test facility will be used in practice.

Fig.3 shows an 80% CDF level of -23.8dB for the rms reconstruction error, and Fig. 4 (top) shows a single example of what the reconstructed array excitation looks like on a false colour grid, for both amplitude and phase, compared to the true faulty array. Also shown in Fig. 4 (bottom) is the case for just one fault (-10dB, 45°) indicating a very low level of rms reconstruction error of -36.2 dB for the 80% CDF point, evidenced by the low background noise to the reconstruction. Comparing these results for array elements of size (0.5λ x 0.7λ) with those of a previous study initially presented in reference [4] which comprised an 8x24 array of element size 0.41λ shows the smaller elements difference field to be weaker and more confined to the projection of the array aperture in the measurement plane, resulting in a 4 fault 80% CDF rms reconstruction error of -25.6dB, several dB better than for the (0.5λ x 0.7λ) element case of Fig. 3.

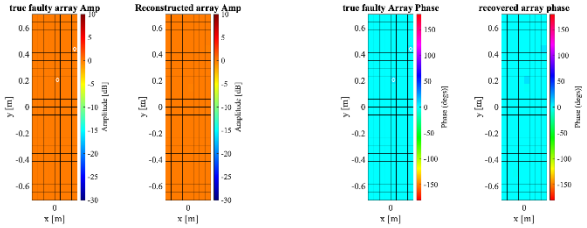

Fig. 5. Reconstruction of an array with two 5.6° phase only faults. Left amplitude, right phase. The white diamonds indicate the true fault locations.

In our previous NF CS work with a large 512 element array, we found several dB improvement in reconstruction rms error by averaging results across six sets of 36 samples. However, no such benefit was found for these smaller 192 element arrays, probably due in part to the small number of element-fails required to achieve our 2% maximum failure rate target. As an indication of the resolution that CS can provide, Fig. 5 shows the reconstruction of an array with two phase-only faults of just 5.6°, representing a least-significant single bit failure of a 6-bit digital phase shifter. The clear identification of the two-phase faults, and lack of background noise, is clearly shown in the figure.

A summary of the NF CS rms amplitude reconstruction error for different levels of element fault is shown in Fig. 6. From this we can see that our target of detecting up to 2% element error (4 faults in this case) can be achieved with just 25 samples with a reasonable -25dB rms reconstruction error. Also shown on the figure is that 49 samples can offer up to six faulty element detection to better than -22dB rms error. For this study we will take forward the 25-sample case that offers the required 2% failure detection and in the next section consider the requirements for a practical implementation using a fixed array of 25 pseudo randomly located NF samples.

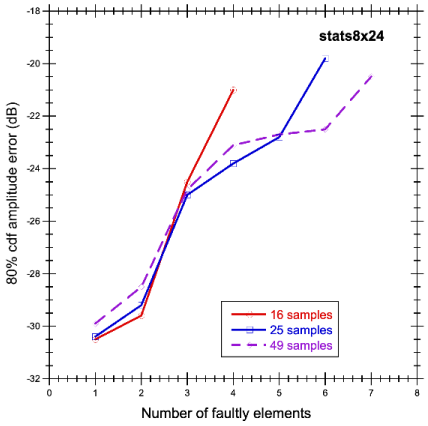

Fig. 6. 80% CDF rms amplitude reconstruction error vs number of faults for the 8x24 array for different numbers of NF samples.

V. A Test System Implementation Using a Planar Array of 25 NF Samples

As stated within the introduction, the aim of this work is to implement a *rapid* production test system for massive MIMO arrays, with an expected manufacturing fault level for the radiating elements at or below 2%. In the previous section we found that just 25 pseudo-randomly located NF samples are required to achieve reasonable reconstruction accuracy for the 8x24 array. Such a system could be implemented using a robotic arm mounted probe to provide the NF samples. However, in a production test environment, when a large number of identical devices need to be tested, it is attractive from a speed perspective to use 25 low-cost probes (for example one based on an absorber nested dual polarisation Vivaldi antenna [22]) arranged on the NF plane and connected via a PIN switch matrix to a Vector Network Analyser (VNA). The absorber nested, low scattering cross-section, well-matched, elements of [22] can be integrated in the overall absorber sheet that the array transmits into thus offering low interference to the AUT. For the low microwave frequencies intended for this work (3.5GHz) such an implementation would be faster, cheaper and more compact than implementing a robotic-arm based scanning probe. However, for smaller scale production testing a robotic-arm is a viable alternative.

As described earlier, *cf.* (Fig. 1), the use of CS in array diagnosis is predicated on measuring the NF difference between the gold antenna and the antenna under test (AUT). In practice this must entail the NF measurement of the gold antenna at the 25 sample points and then the placing of the AUT in *exactly the same* location to measure the same 25 NF samples. The use of a fixed array for the sample point will help the accuracy of this process but we need to understand the tolerance of the CS process to both transverse location errors (x,y) between the gold and AUT antennas as well as the longitudinal (z) ones. We first consider x,y location errors and in Fig.7, by way of an illustration, we show the effect on the full NF difference pattern between exact co-location and an $x = y = 0.01\lambda = 0.9$mm transverse translation of the AUT with respect to the gold antenna.

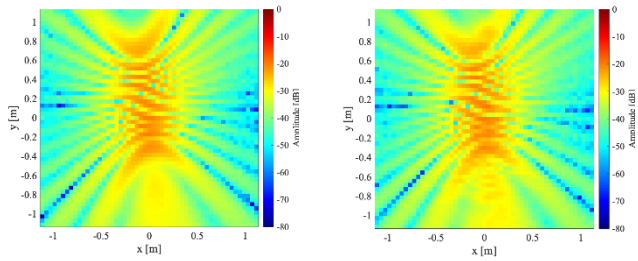

Fig. 7. The full NF difference pattern for two faulty elements: left full alignment between gold and AUT; right x=y = 0.01λ translation between gold and AUT.

The 80% CDF rms reconstruction error for the aligned case is -29.4dB and for the transverse misaligned case is -28.6dB, which is an acceptably small level of degradation and represents a misalignment error in x and y of 0.9 mm. A well-designed test rig will easily be able to achieve this [3, 15]. We next consider a longitudinal (z) location error between gold and AUT. Fig. 8 shows the NF difference pattern for the case for a z error of $0.002\lambda = 0.17$mm (left) and $0.01\lambda = 0.9$mm (right), the corresponding 80% CDF rms reconstruction errors are -28.3 dB and -21.1 dB. Clearly the tolerance to longitudinal alignment of the CS measurement system is *much* more critical than that of transverse alignment.

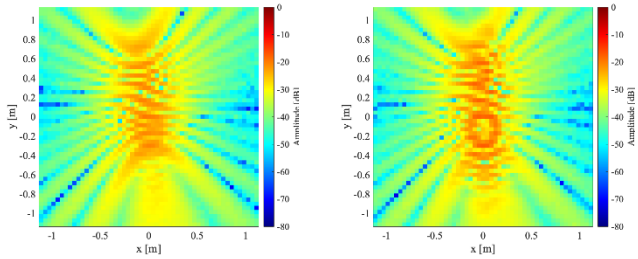

Fig. 8. The full NF difference pattern for two faulty elements: left z misalignment between gold and AUT of 0.002λ; right z misalignment between gold and AUT of 0.01λ.

This observation, for antennas with main beams aligned predominantly in the z-axis is consistent with the findings of standard planar near-field scanning where is it noted that measurement planarity is generally a more significant term within the overall facility uncertainty budget than the corresponding transverse effect [25, 3, 15]. This result is not surprising when we realise that any z translation between gold and AUT antennas is effectively a phase change across the AUT array, so every element has effectively a phase fault added to it, rendering the system non-sparse. Even if we could engineer a mechanical alignment system that could be accurate to within 0.17mm ($0.002\lambda = 0.7°$), such a phase change could be easily generated by thermal drift of the RF subsystem between the gold and AUT measurements. This is a problem that has not been highlighted before in the significant number of publications on CS array antenna diagnosis and is a factor that could render the approach entirely ineffective.

For operation at higher frequencies the mechanical alignment requirements become more stringent with the shorter wavelength, and thus the position repeatability of the robotic arm becomes more problematic making the array of probes solution a more viable approach.

In this section we propose and verify through simulation a scheme to overcome the *z* tolerance issue highlighted in the previous section. The proposed approach is as follows:

- Count cells of the reconstructed array with amplitude < ± 1 dB of the known gold array excitation and assume there is no error on these cells.
- Similarly, count cells of the reconstructed array phase < ± 5° of the known gold array excitations and assume there is no error on these cells.
- Plot these values as a scan through various values of *z* deflection are tried in the CS code over a range of $z = \pm 0.05\lambda$ with a step size of 0.0025λ.
- Pick the set that has the largest count (*i.e.* minimum number of faulty elements) to give an estimate of the true *z* error.

Here, z-span and step size were predicated on knowledge of the anticipated upper-bound positioning tolerance that is achievable using conventional precision machined interfaces, and alignment dowel pins, as well as expected RF subsystem thermal drift. Fig. 9 shows this for the case for 2 faults, 25 samples and a z-location error set at 0.03λ. We can see from this case that the peak number of error free cells is found at the correct *z*-location value of 0.03λ for both the amplitude and phase count. It is also possible the amplitude and phase peak counts do not coincide (for example amplitude count finds 0.03λ, phase count finds 0.0275λ).

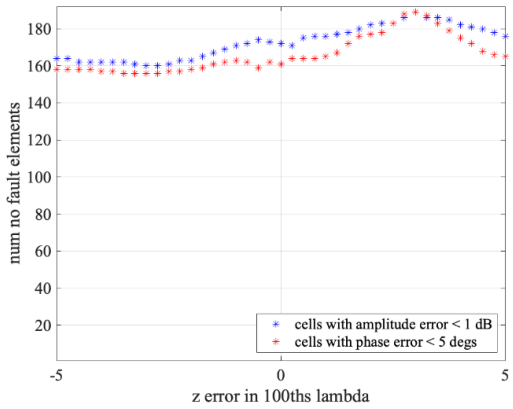

Fig. 9. Number of non-faulty elements vs z-location error to locate the predicted value of the *z*-location error (true value = 0.03λ). 2 faults and 25 samples.

In this case we compute the recovered array excitations for both *z*-location values and average the result. We have tried several values for the amplitude count criteria (±1dB used above) and the phase count criteria (±5° used above) and found that ±1dB and ±10° gave the most consistent results. It is also clear from Fig. 9 that CS does indeed 'work' to some extent in that over a range of *z* position errors it can find around 160 fault free array elements, but the true answer is 190, and this is only achieved when the correct value of *z* is chosen. For this application we are looking for high accuracy and especially low false alarm rates hence this is an issue that needs to be resolved.

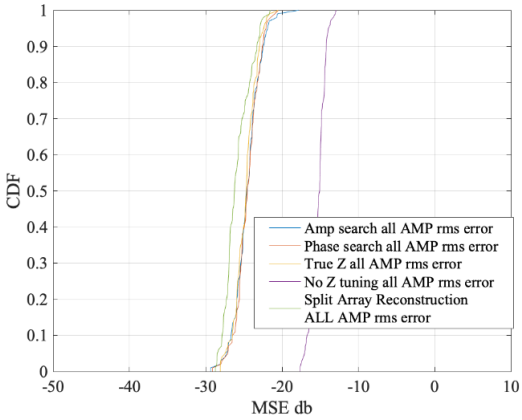

Fig. 10. CDF rms amplitude reconstruction error for z-location error process (25 samples 4 randomly located faults) taken over 50 sets of different fault locations. Gold and AUT antennas are misaligned in *z* by 0.03λ

Fig.10 shows the CDF rms amplitude reconstruction error for the above *z*-location error process when repeated 100 times with 25 fixed samples, and 4 randomly located faults. Shown on this figure are the CDF results for the following cases of reconstructing the array excitations using: the z-location error detected using the amplitude counts; the *z*-location error detected using the phase counts; the true value of *z*-location error (0.03λ in this case); the case with no attempt at *z*-location error correction. Clearly, the recovery process works correctly, and it is worth noting the 10dB improvement in the amplitude reconstruction error that this process provides.

VII. Improving Accuracy Using Partial Excitation of the Array

We can further improve the accuracy of this system by adding additional measurements that excite just parts of the array, perform the diagnostics on those parts, and then combine the results and take an average over the set of predicted excitations. We demonstrate this approach using the following example:

- First, excite the full array and undertake reconstruction process described in the previous section. This provides two sets of array excitation predictions, one based on the amplitude-based *z*-location error search, and one for the corresponding phase-based search.
- Split the array into two by exciting just the bottom 12 rows of elements and repeat the reconstruction process with all 25 NF sample points.
- We then repeat this by exciting just the top 12 rows, again with all 25 NF samples. From the predicted excitations of these two sub-arrays, we can combine the result to obtain a second set of recovered excitations for the full array. Again, there are two sets of array excitation predictions from the amplitude and phase-based *z*-location searches.
- Additionally, we can repeat this subarray process, but this time using just the bottom and top half of the sampling array when exciting the bottom and top half of the array respectively. From the predicted excitations of these two sub-arrays, we can combine the result to get a third set of recovered excitations. Again, there are two sets of array

excitation predictions from the amplitude and phase-based *z*-location searches.

- This provides in total 6 sets of array amplitude and phase excitation predictions, from which we can obtain a single averaged reconstruction for the AUT.

We call this procedure *Split Array Reconstruction*, and undertake this process 100 times with 25 fixed samples and 4 randomly located faults and in Fig. 10 plot the resulting CDF rms amplitude reconstruction error. Compared to the results of purely measuring the full array, we see an improvement in the CDF rms reconstruction errors of several dB over the full range of CDF values, *i.e.* the left most trace in the Fig 10 labelled: "Split Array Reconstruction ALL AMP rms error".

Controlling the array excitation during production testing is entirely viable as the array manufacturer will have unconstrained access to test the arrays with different beam steers and thus have access control of the amplitude and phase of each element. Indeed, most MIMO arrays are made up of sub array 'tiles" and so in the case of our 24x8 array each tile may be 8x8 elements, which would easily lend itself to the proposed Split Array Reconstruction with different combination of these 8x8 tiles turned on or off.

To see what this looks like for a particular reconstruction, Fig. 11 compares the array amplitude and phase reconstruction when the *z*-location error procedure from the previous section is used (left) and when added to this is the *Split Array Reconstruction* process (right). Although, as mentioned above the CDF is improved by just a few dB, the reconstructed excitations are clearly less noisy for the *Split Array Reconstruction.*

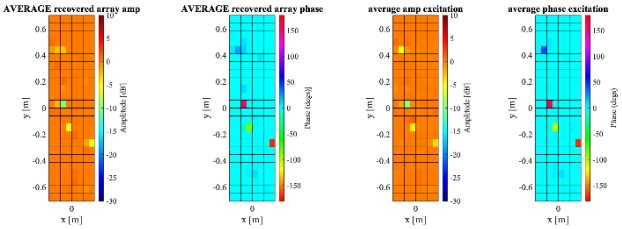

Fig. 11. Reconstructed array amplitude (a), and phase (b) for average excitation when z-location error procedure of section VI is used. Added to this is the Split Array Reconstruction process amplitude (c) and phase (d).

With the ability to accurately detect the exact fault levels limited, it is possible to create an element level pass/fail fault detection process by looking for failed elements based on using the amplitude and phase error search we used for the *z*-location error process described above. The devised procedure is as follows:

1. Consider each cell of the reconstructed array amplitude with excitation > ± 1 dB of the *gold* array to represent a faulty cell and set value to one, otherwise for the faultless cell set to zero. This provides one set of binary fault predictions for the array.
2. Repeat the above process, this time with excitations > ± 10° representing a faulty cell, providing a second set of fault predictions.
3. The previous two steps are then repeated for different search levels of > ±2dB and >± 20°, and again for > ±3dB and >± 30°.

By adding these three sets of binary pass/fail for each array element, a fault likelihood level is created with a range of 0 to 3, with 3 representing a cell most likely in error. This process is performed for both the array amplitude reconstruction and the phase reconstruction. These two results are kept separate as the CS process is effective for differentiating between an array element amplitude fault, and a phase fault, as demonstrated earlier within the text, *cf.* Fig. 5.

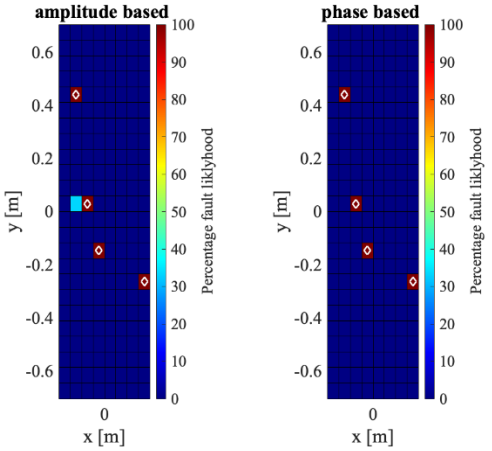

Fig. 12. Array element fault likelihood when based on an amplitude fault search (left) and a phase fault search (right). The white diamonds indicate the true fault locations.

Thus, a likelihood of an amplitude fault, a phase fault, or a fault on both is provided. For the *Split Array Reconstruction* results shown in Fig. 11, the resulting fault likelihood is shown in Fig. 12 when based on an amplitude fault search (left) and a phase fault search (right). Taking a 50% likelihood as a true fault we note that both the amplitude and phase-based searches indicate the correct four faults and their true location.

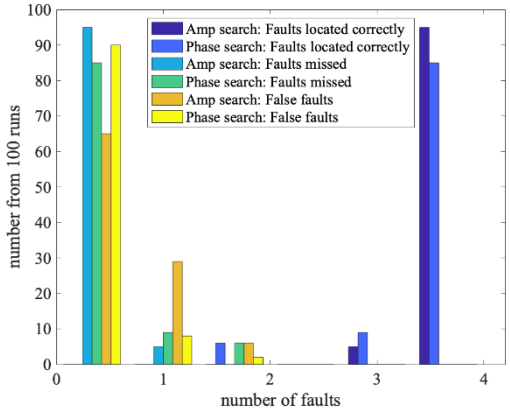

Fig. 13. Bar-chart showing the fault likelihood process performance in terms of: faults correctly located, faults missed, and faults falsely identified. Case of 25 fixed samples and 4 randomly located faults. Statistics taken over 100 runs with different sets of fault locations

A statistical view of the performance of this procedure is shown in the bar chat of Fig. 13, where the Split Array Reconstruction and fault likelihood process is undertaken 100 times with 25 fixed samples and 4 randomly located faults (shown listed in the inset to Fig. 2). Fig 13 shows that 95% of the time the 4 faults are located correctly for the amplitude-based search, with 85% for the phase-based search. Missed faults are found to be less than 10% for both amplitude and phase-based searches. False faults are <10% for phase-based

searches but single false faults can occur up to 30% of the time for amplitude-based searches. Fig. 14 shows the bar-chart for the case of just 2 randomly located faults where the fault location process is near perfect.

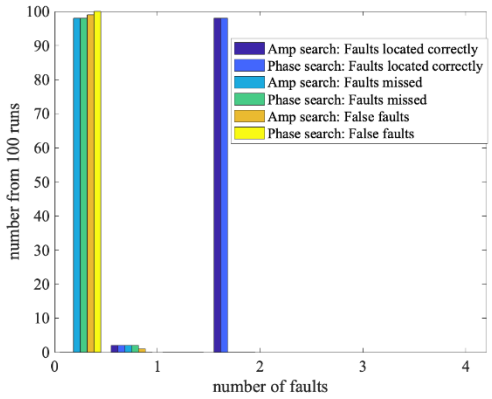

Fig. 14. Bar-chart showing the fault likelihood process performance in terms of: faults correctly located, faults missed, and faults falsely identified. Case of 25 fixed samples and 2 randomly located faults. Statistics taken over 100 runs with different sets of fault locations.

Fig. 15 shows the bar-chart for the case of just a single phase only fault of 22.5° randomly located faults where the fault location process is near perfect, with a correct identification of the fault occurring 88% of the time. Shown inset to this figure is a single example array excitation reconstruction from the 100 randomly located fault showing clear low noise reconstruction. Repeating the process for a single phase only fault of 11.2° gave poor results. However, running the process for the case when the AUT has a single randomly located -3dB fault over 100 runs lead to a 75% success rate in correctly locating the fault.

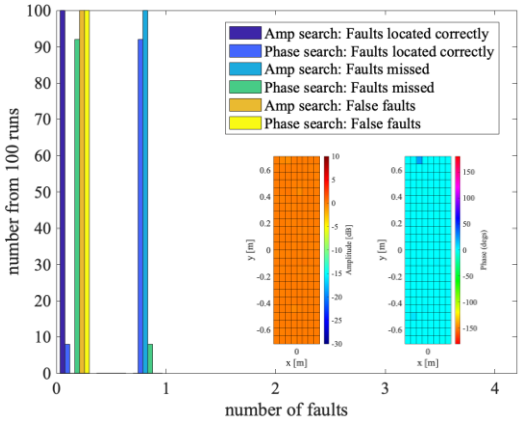

Fig. 15. Bar-chart showing the fault likelihood process performance in terms of: faults correctly located, faults missed, and faults falsely identified. Case of 25 fixed samples and one randomly located phase only fault of 22.5°. Inset to figure is a single example of the amplitude and phase reconstruction. Statistics taken over 100 runs with different sets of fault locations

For cases where there are more than 4 faults, the performance rapidly tails off with 75% success rate of locating all 4 faults correctly dropping to 55% for the case of 6 faults. However, when a complete row of the array is faulty, as when a beamformer has a row out of calibration, this can be reliably detected, as in the example shown in Fig.16 where a row fault of 22.5° is picked up well by the fault likelihood process. In practice this means that even if the exact elemental faults are not perfectly determined, sufficient warning is provided to the user that the production antenna requires further remedial action.

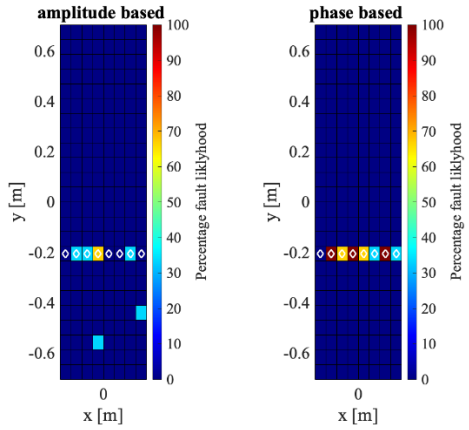

Fig. 16. Array element fault likelihood for case of a beamformer row fault of 22.5°: amplitude fault search (left) and a phase fault search (right). The white diamonds indicate the true fault locations.

Continuing to look at the phase reconstruction performance of the *Split Array Reconstruction*, Fig. 17 compares the rms phase reconstruction error across the whole array along with that for just the fault elements for the case of both 2 and 4 faults. Clearly, the accuracy of the reconstruction improves significantly as the number of faults drop, as the problem CS solves becomes more sparce. Running the *Split Array Reconstruction* process for the case when the AUT has no faults over 100 times showed a 100% no fault detection, and 0% false alarm rate, Fig. 18 shows a typical reconstructed array excitation.

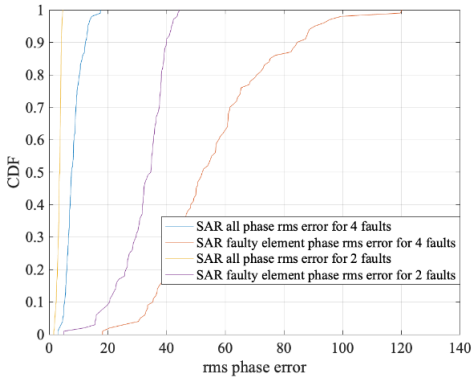

Fig. 17. CDF rms phase reconstruction error for the Split Array Reconstruction (SAR) process for both the 4 fault and 2 fault case (25 samples). Statistics taken over 100 runs with different sets of fault locations

Finally, we summarise the performance of the *Split Array Reconstruction* (SAR) process over a range of faults from 0 to 6, with Fig. 19 showing the 80% CDF rms error amplitude and phase of the reconstructed array across the whole antenna compared to the true faulty antenna (solid red and blue lines), the data being taken over 100 runs of randomly located faults. These plots clearly show the accuracy of the reconstruction increases as the number of faults reduces.

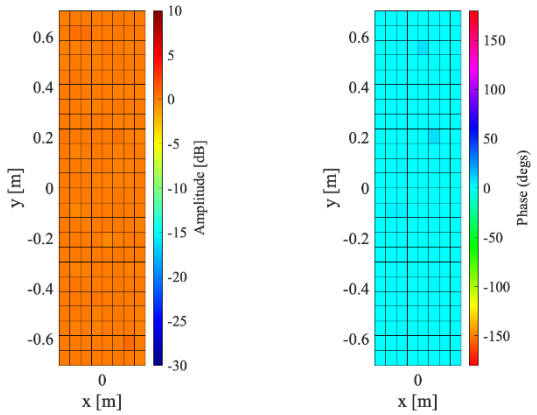

Fig. 18. Reconstructed array excitation for zero fault case. Left: amplitude, right: phase.

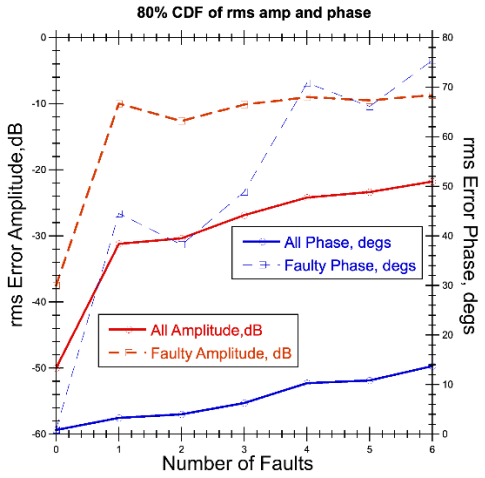

Fig. 19. Summary of the reconstruction errors compared to the true faulty array for the *Split Array Reconstruction* process over a range of faults. Solid lines are 80% CDF rms error amplitude across the whole array; dotted lines are the 80% CDF rms error amplitude across just the faulty elements.

Also shown in Fig. 19 is the corresponding rms error amplitude and phase across just the faulty elements (dotted red and blue lines). Here we see that the accuracy of amplitude reconstruction across most fault levels is about -10dB, and with no faults it is down to -37dB. For the corresponding faulty element phase reconstruction accuracy, the value fairly steadily decreases from a maximum of 75° at 6 faults to 0.9° at zero faults.

VIII. Summary and Conclusion

In taking the CS technique for array diagnosis to a practical level through measurement simulation and undertaking a tolerance study we have identified a fundamental flaw in the method, this being the longitudinal alignment tolerance required between the *gold* reference antenna and AUT. To not significantly impact the reconstruction accuracy this z-axis alignment needs to be better than 0.002λ or 0.17mm at our working frequency of 3.5GHz. To compound the problem this is an *electrical path length difference* tolerance, so even if the mechanical *z*-axes are *both* perfectly aligned, this 0.002λ path length change can be produced by a thermal drift within the RF subsystem between the gold antenna measurement and the AUT measurement, and is a drift of only 0.7°. As far as the authors are aware, this issue has not been exposed in the open literature before and makes the basic gold/AUT difference pattern CS based array diagnosis process unusable in practice without some form of mitigation being implemented.

However, in this paper we have proposed and verified through simulation a process by which this problem can be overcome and recover nearly all the expected performance from the basic CS array diagnostic technique. The performance analysis for the specific massive MIMO array considered here suggests that fault levels up to 2% can be well identified, with performance tailing off as the number of faults increase and hence the problem becomes progressively less sparce. Furthermore, we obtained similar results for a 12x16 which has the same number (192) of radiating elements. We have also looked at larger arrays 20x28 (512 elements) and this 2% rule continues to apply.

The speed of this array diagnosis procedure is its major benefit, a single run of the *Split Array Reconstruction process* takes 18 seconds (on an iMAC 3.1 GHz Quad-Core Intel Core i5) with MATLAB simulation code. The measurement processing time is equally short when the 25 randomly placed fixed NF probes are connected via a PIN switch matrix to a Vector Network Analyser (VNA), even if we run the VNA at a 10Hz bandwidth to maximise the noise suppression. Note that throughout all the simulation work we have used a -60dB level of noise for all the 'measured' signals in our simulations. However, in practice, our RF link budget calculations suggests that achieving a circa 80 dB dynamic range for a 100 Hz IF bandwidth is realistic. Assuming the entire RF measurement takes circa 10 seconds, a very conservative estimation that is in part predicated upon the switching and settling time of the massive MIMO antenna, the whole test could take less than 30 seconds. For tested devices that show faults that can be corrected, re-testing of the AUT, this time with fewer faults (and hence more sparsity) will provide even more accurate determination of any remaining faults *cf.* Fig. 19. With such short test times, several rounds of correction and re-test become easily viable, and we have shown that a single 22.5° can be detected so convergence to a near perfect array becomes possible.

It is important to emphasise that because the CS process is based on the difference between the gold and AUT near-field, the actual excitation used for the array elements is not important, so any excitation in amplitude and phase can be used. Indeed in [16, 17] we show that the system works correctly when diagnosing a scanned beam in azimuth and elevation. Thus, a practical implementation of the proposed system may well employ a number of beam directions and shapes.

Comparing this proposed system to conventional planar NF measurement at Nyquist sampling and subsequent back projection to the array aperture would require 1,537 NF samples. This is based on a NF sampling region size of 26.5λ×14.5λ, which would provide FF azimuth and elevation patterns valid out to 60° [3]. Our proposed method requiring just 25 samples represent 1.6% of the amount required by the classical Nyquist sampling and conventional aperture

diagnostics.

REFERENCES

[1] Wonil Roh, "5G Mobile Communications for 2020 and Beyond - Vision and Key Enabling Technologies," *IEEE WCNC 2014 Keynote*, Apr. 2014.

[2] Z. Pi and F. Khan, "An introduction to millimeter-wave mobile broadband systems," *IEEE Commun. Mag.*, vol. 49, no. 6, pp. 101–107, Jun. 2011.

[3] S.F. Gregson, J. McCormick, C.G. Parini, "Principles of Planar Near-Field Antenna Measurements, 2nd Edition", IET Electromagnetic Waves series 53, ISBN 978-1-83953-699-1, July 2023.

[4] C.G. Parini, S.F. Gregson, "Compressive Sensing Applied to Production Testing of Array Antennas using a Robotic Arm and Very Sparsely Sampled Near-Field Measurements", 18th European Conference on Antennas and Propagation (EuCAP), 17-22 March 2024, Glasgow, Scotland.

[5] D. L. Donoho, "Compressed sensing," IEEE Transactions on Information Theory, vol. 52, no. 4, pp. 1289–1306, April 2006. 2, 39, 40.

[6] E. J. Candes and T. Tao, "Near-optimal signal recovery from random projections: universal encoding strategies?" IEEE Transactions on Information Theory, vol. 52, no. 12, pp. 5406–5425, Dec. 2006. 2, 40.

[7] E. J. Candes, J. Romberg, and T. Tao, "Robust uncertainty principles: Exact signal reconstruction from highly incomplete frequency information," IEEE Transactions on Information Theory, vol. 52, no. 2, pp. 489–509, 2006. 2, 39,40.

[8] S. Foucart and H. Rauhut, A mathematical introduction to compressive sensing. Springer, 2013. 39, 40, 41, 48.

[9] Z. Chen, S.F. Gregson, Y. Wang, "Novel Application of Compressed Sensing in Cylindrical Mode Filtering for Far-Field Antenna Measurements", Antenna Measurement Techniques Association Annual Symposium, Seattle, USA, October 2023.

[10] S.L. Brunton, J.N. Kutz, "Data-Driven Science and Engineering", second edition, Cambridge University Press, 2022, ISBN 978-1-009-09848-9

[11] B. Fuchs, L. Le Coq, S. Rondineau, and M. D. Migliore, "Fast antenna far field characterization via sparse spherical harmonic expansion," IEEE Transactions on Antennas and Propagation, vol. 65, no. 10, pp. 5503–5510, 2017. 3, 42, 48

[12] R. Cornelius, D. Heberling, N. Koep, A. Behboodi, and R. Mathar, "Compressed sensing applied to spherical near-field to far-field transformation," in138 10th European Conference on Antennas and Propagation (EuCAP). IEEE, 2016, pp. 1–4. 3, 42.

[13] B. Fuchs, L. Le Coq, S. Rondineau, and M. D. Migliore, "Compressive sensing approach for fast antenna far field characterization," in 12th European Conference on Antennas and Propagation (EuCAP). IEEE, 2018. 3, 42, 48

[14] L. C. Potter, E. Ertin, J. T. Parker, and M. Cetin, "Sparsity and compressed sensing in radar imaging," Proc. IEEE, vol. 98, no. 6, pp. 1006–1020, 2010.

[15] C. G. Parini, S. F. Gregson, J. McCormick, D. Janse van Rensburg, T.S. Eibert, "Theory and Practice of Modern Antenna Range Measurements", (2nd expanded edition), *IET Press*, 2020, in 2 volumes, ISBN 978-1-83953-126-2 and ISBN 978-1-83953-128-6.

[16] S.F. Gregson, Z. Qin, C.G. Parini, "Compressive Sensing in Massive MIMO Array Testing: A Practical Guide", IEEE Transactions on Antennas and Propagation, 2022, Volume: 70, Issue: 9

[17] C.G. Parini, S.F. Gregson, "Compressive Sensing Applied to Planar Near-Field Based Array Antenna Diagnostics for Production Testing", AMTA 2023, October 2023, Seattle, USA.

[18] T.K. Sarkar, M. Salazar-Palma, M.D. Zhu, H. Chen, "Modern Characterization of Electronic Systems and its Associated Metrology", IEEE Press, 2021, ISBN 978-1-119-07646-9.

[19] Michael Grant and Stephen Boyd, "CVX: Matlab Software for Disciplined Convex Programming, Version 2.0 beta," http://cvxr.com/cvx, September 2013.

[20] YALL1 basic solver code: Y. Zhang, J. Yang, and W. Yin. Available for download from https://github.com/andrewssobral/YALL1, last accessed 4th July 2024.

[21] E. van den Berg and M. P. Friedlander, "SPGL1: A Solver for Large-scale Sparse Reconstruction", https://friedlander.io/spgl1/, December 2019.

[22] ETS-Lindgren, Model 3165-01 Absorber Nested Dual-Polarized Dual-Vivaldi Array, data sheet, https://www.ets-lindgren.com/datasheet/antennas/absorber-nested-dual-polarized-dual-vivaldi-array-antenna/4004/400401, last accessed 4th July 2024.

[23] L. J. Foged, L. Scialacqua, F. Saccardi, J. L. A. Quijano, G. Vecchi and M. Sabbadini, "Practical Application of the Equivalent Source Method as an Antenna Diagnostics Tool [AMTA Corner]," in IEEE Antennas and Propagation Magazine, vol. 54, no. 5, pp. 243-249, Oct. 2012, doi: 10.1109/MAP.2012.6348170.

[24] Sierra Castaner, Manuel; Foged, Lars J. (ed.): 'Post-processing Techniques in Antenna Measurement' (Electromagnetic Waves, 2019) DOI: IET Digital Library, https://digital-library.theiet.org/content/books/ew/sbew529e

[25] E.B. Joy, R.E. Wilson, "A Simplified Technique for Probe Position Error Compensation in Planar Surface Near Field Measurements" 4th Annual Symposium and Meeting of the Antenna Measurement Techniques Association, October 1982.

Professor Clive G. Parini, FREng. (M'96) Joined Queen Mary as Lecturer in 1977, promoted to Reader in 1990, promoted to Professor in 1999 and is currently Professor of Antenna Engineering in the Antenna & Electromagnetics Research Group. He has published over 400 papers on research topics including array mutual coupling, array beam forming, antenna metrology, microstrip antennas, millimetrewave compact antenna test ranges, millimetrewave integrated antennas, metamaterials and on-body communications. In 1990 he was one of three co-workers to receive the IEE Measurements Prize for work on near field reflector metrology. In 2002, along with several co-workers, he was awarded the BAE SYSTEMS Chairman's Bronze Award for Innovation for work on microwave near-field metrology. 2008 he co-authored the book entitled "Principles of Planar Near-Field Antenna Measurements" (now in its second 2023 edition) and in 2014 co-authored the book entitled "Theory and Practice of Modern Antenna Range Measurements" (now in its second 2021 edition). He is a Fellow of the IET and a past. He is a Fellow of the IET and a past member and Chairman of the IET Antennas & Propagation Professional Network Executive Team. He is a past member of the editorial board and past Honorary Editor for the IET Journal *Microwaves, Antennas & Propagation*. In 2009 he was elected a Fellow of the Royal Academy of Engineering

Professor Stuart Gregson has in excess of twenty five years of experience working in the space, aerospace and communications sectors and is currently Director of Operations and Research at Next Phase Measurements, and an honorary visiting professor in the School of Electronic Engineering and Computer Science at Queen Mary University of London. He received his BSc degree in Physics in 1994 and his MSc degree in Microwave Solid State Physics in 1995 both from the University of Portsmouth. He received his PhD degree in 2003 from Queen Mary University of London with near-field antenna measurements and statistical pattern recognition as his main subject areas. From his time with: Airbus, Leonardo, NSI-MI and the National Physical Laboratory Prof. Gregson has developed special experience with near-field antenna measurements, finite array mutual coupling, computational electromagnetics, installed antenna and radome performance

prediction, compact antenna test range design & simulation, electromagnetic scattering, 5G OTA measurements and has published numerous peer-reviewed research papers on these topics regularly contributing to and organizing industrial courses on these subject areas. At the end of 2007 he was the lead author of the research text Principles of Planar Near-Field Antenna Measurements, and in 2014 he co-authored a second text, Theory and Practice of Modern Antenna Range Measurements both of which are in 2nd editions. He is a Fellow of the Antenna Measurement Techniques Association, a Fellow of the Institution of Engineering and Technology, a Fellow of the Institute of Physics and is a chartered Engineer and Physicist. In 2018, Prof. Gregson was elected to the AMTA Board of Directors where he served first as Treasurer and then as Vice President.